NUMERICAL COMPUTATION OF VISCOUS BLUNT BODY FLOWS WITH A PLANAR IMPINGING SHOCK*

By Terry L. Holst and John C. Tannehill
Iowa State University
and
John V. Rakich
NASA Ames Research Center

SUMMARY

Two- and three-dimensional, viscous blunt body flows with planar impinging shocks are computed using an explicit, time-dependent, finite-difference method to solve the complete set of Navier-Stokes equations. The bow shock is treated as a discontinuity, while all interior shock layer detail such as shear layers, shock waves, jets and the wall boundary layer are automatically captured in the solution. Numerical results are presented for cases in which planar shock waves of different strengths and orientations are allowed to impinge on the flow field surrounding an infinite cylinder resulting in two- and three-dimensional shock interference patterns. The numerical results are compared with experiment.

INTRODUCTION

An extraneous shock wave impinging on a blunt body in a hypersonic flow has been observed to greatly increase both the heat transfer rate and pressure near the impingement point (refs. 1 and 2). Flow fields of this type may occur on hypersonic vehicles such as the Space Shuttle.

---

*This work was supported by NASA Ames Research Center under Grant NGR 16-002-038 and the Engineering Research Institute, Iowa State University, Ames, Iowa.

The intense heating and high pressures occur over a small region where a disturbance, originating at the intersection of the impinging shock and bow shock, strikes the body. The disturbance may be a free shear layer, a supersonic jet, or a shock wave depending on the strength and location of the impinging shock and the shape of the body. Edney (ref. 1) has described six different types of shock interference patterns which can occur.

In the present study, both two- and three-dimensional shock impingement flow fields have been numerically computed. In these computations, the impinging shock is planar and intersects the bow shock surrounding an infinite cylinder (fig. 1). In the two-dimensional case the intersection line is parallel with the axis of the cylinder (z-axis), and consequently the flow in each z-plane is identical. This configuration can occur in hypersonic inlets. In the three-dimensional case, the intersection line is curved and is not parallel with the cylinder axis. This configuration can occur when the bow shock from the nose of a vehicle strikes the wing leading edge bow shock.

The numerical results of this study were computed using a time-dependent, finite-difference method to solve the complete set of Navier-Stokes equations for a laminar, compressible flow. The time-dependent approach was chosen because a subsonic region exists in the two-dimensional case and may exist in the three-dimensional case. Since the governing time-dependent equations remain a hyperbolic-parabolic set for both subsonic and supersonic flows, all cases can be solved as an initial-value problem where the steady-state solution is approached asymptotically with time.

SYMBOLS

e	=	specific internal energy
E	=	total energy
k	=	coefficient of thermal conductivity
M	=	Mach number
p	=	pressure
Pr	=	Prandtl number
q_j	=	heat flux vector
r, θ, z	=	cylindrical coordinates
r_b	=	body radius
r_s	=	shock radius
Re_D	=	Reynolds number based on cylinder diameter
t	=	time
T	=	temperature
u_r, u_θ, u_z	=	velocity components
β	=	stretching parameter
γ	=	ratio of specific heats
λ	=	sweep angle
μ	=	coefficient of viscosity
ρ	=	density
τ_{ij}	=	shear stress tensor

subscripts

∞	=	freestream condition
cyl	=	swept infinite cylinder value
stag	=	no impingement stagnation value

GOVERNING EQUATIONS

The equations governing the flow of a compressible, viscous fluid in the absence of body forces and electromagnetic effects can be written in the following weak conservation-law form using three-dimensional cylindrical coordinates:

$$\frac{\partial U}{\partial t} + \frac{\partial F}{\partial r} + \frac{\partial G}{\partial \theta} + \frac{\partial H}{\partial z} + D = 0 \tag{1}$$

where

$$U = r \begin{bmatrix} \rho \\ \rho u_r \\ \rho u_\theta \\ \rho u_z \\ E \end{bmatrix} \tag{2a}$$

$$F = r \begin{bmatrix} \rho u_r \\ \rho u_r^2 + p - \tau_{rr} \\ \rho u_r u_\theta - \tau_{r\theta} \\ \rho u_r u_z - \tau_{rz} \\ (p+E)u_r - \tau_{rr}u_r - \tau_{r\theta}u_\theta - \tau_{rz}u_z + q_r \end{bmatrix} \tag{2b}$$

$$G = \begin{bmatrix} \rho u_\theta \\ \rho u_r u_\theta - \tau_{r\theta} \\ \rho u_\theta^2 + p - \tau_{\theta\theta} \\ \rho u_\theta u_z - \tau_{\theta z} \\ (p+E)u_\theta - \tau_{r\theta}u_r - \tau_{\theta\theta}u_\theta - \tau_{\theta z}u_z + q_\theta \end{bmatrix} \tag{2c}$$

$$H = r \begin{bmatrix} \rho u_z \\ \rho u_r u_z - \tau_{rz} \\ \rho u_\theta u_z - \tau_{\theta z} \\ \rho u_z^2 + p - \tau_{zz} \\ (p+E)u_z - \tau_{rz}u_r - \tau_{\theta z}u_\theta - \tau_{zz}u_z + q_z \end{bmatrix} \tag{2d}$$

$$D = \begin{bmatrix} 0 \\ -(\rho u_\theta^2 + p - \tau_{\theta\theta}) \\ \rho u_\theta u_r - \tau_{r\theta} \\ 0 \\ 0 \end{bmatrix} \tag{2e}$$

$$E = \rho\left(e + \frac{u_r^2 + u_\theta^2 + u_z^2}{2}\right) \tag{2f}$$

The Navier-Stokes expressions for the components of the shear stress tensor and heat flux vector have been used in this study and are given by:

$$\tau_{rr} = \mu e_{rr} - \frac{1}{3}\mu(e_{rr} + e_{\theta\theta} + e_{zz}) \qquad \tau_{r\theta} = \tau_{\theta r} = \mu e_{r\theta}$$

$$\tau_{\theta\theta} = \mu e_{\theta\theta} - \frac{1}{3}\mu(e_{rr} + e_{\theta\theta} + e_{zz}) \qquad \tau_{rz} = \tau_{zr} = \mu e_{rz}$$

$$\tau_{zz} = \mu e_{zz} - \frac{1}{3}\mu(e_{rr} + e_{\theta\theta} + e_{zz}) \qquad \tau_{\theta z} = \tau_{z\theta} = \mu e_{\theta z}$$

$$e_{rr} = 2\frac{\partial u_r}{\partial r} \qquad e_{r\theta} = \frac{1}{r}\frac{\partial u_r}{\partial \theta} + \frac{\partial u_\theta}{\partial r} - \frac{u_\theta}{r} \tag{3}$$

$$e_{\theta\theta} = \frac{2}{r}\frac{\partial u_\theta}{\partial \theta} + 2\frac{u_r}{r} \qquad e_{\theta z} = \frac{\partial u_\theta}{\partial z} + \frac{1}{r}\frac{\partial u_z}{\partial \theta}$$

$$e_{zz} = 2\frac{\partial u_z}{\partial z} \qquad e_{rz} = \frac{\partial u_z}{\partial r} + \frac{\partial u_r}{\partial z}$$

$$q_r = -k \frac{\partial T}{\partial r}$$

$$q_\theta = -\frac{k}{r} \frac{\partial T}{\partial \theta}$$

$$q_z = -k \frac{\partial T}{\partial z}$$

For the two-dimensional problem the crossflow (z-component) terms are omitted.

To complete this set of equations the perfect gas equation of state is used. In addition, Sutherland's equation and a constant Prandtl number assumption are used to compute coefficients of viscosity (μ) and thermal conductivity (k).

Equation (1) is transformed from the physical domain (r, θ, z, t) into the computational domain (x, y, z, t) using the following independent variable transformation:

$$\begin{aligned} x &= f\left(\frac{r_s - r}{r_s - r_b}\right) \\ y &= \theta \\ z &= z \\ t &= t \end{aligned} \tag{4}$$

This transformation maps the z-plane between the bow shock and the blunt body into a rectangular region and stretches the radial distribution of grid points according to the function f. The function f chosen for all cases considered here is given by (ref. 3):

$$f(a) = \frac{\ell n \left(\frac{\beta + a}{\beta - a}\right)}{\ell n \left(\frac{\beta + 1}{\beta - 1}\right)} \tag{5}$$

Equation (5) refines the grid near the body and thus permits better boundary layer resolution. The parameter β controls the amount of refinement and has a practical range between 1 and 2 with the smaller values giving larger amounts of refinement.

NUMERICAL METHOD

Finite-Difference Scheme

Equation (1) is solved by MacCormack's explicit finite-difference method (ref. 4). This method is composed of a predictor-corrector sequence which is second-order accurate in both space and time. For this method to remain stable the allowable time step is limited by the CFL condition. To ensure numerical stability in regions of large gradients, a fourth-order smoothing term (ref. 3) is applied in each spatial direction for both the predictor and corrector steps.

Boundary Conditions

Two-Dimensional. — The wall boundary conditions are determined by specifying an isothermal wall, a zero normal pressure gradient and the no slip condition. The bow shock forms one boundary of the computational region and its location at each time step is determined using a predictor-corrector method (ref. 3). Flow variables at the row of grid points just inside the bow shock are obtained by applying the exact shock jump relations (Rankine-Hugoniot equations). The impinging shock is introduced at the bow shock by discontinuously changing the freestream conditions across the intersection point.

The tangential outflow boundaries, both top and bottom, are treated with second-order extrapolations. These boundary conditions are stable provided the outflow Mach number in the inviscid region of the shock layer is supersonic.

Three-Dimensional. – The boundary conditions for the three-dimensional case are identical to those of the two-dimensional case with the following exceptions. The geometry in the three-dimensional case permits a plane of symmetry to be assumed along the stagnation line across which reflective boundary conditions are used. The flow conditions at the inflow plane in the crossflow direction are held fixed for all time equal to the conditions from a swept infinite cylinder solution calculated prior to the shock impingement solution. The flow conditions at the outflow boundary are determined using a zeroth-order extrapolation in the crossflow direction.

RESULTS

Two-Dimensional

Two-dimensional results were computed with the following freestream conditions:

$$\begin{aligned} M_\infty &= 4.6 & p_\infty &= 14.93\ N/m^2 \\ Re_{D\infty} &= 10{,}000 & T_\infty &= 167\ ^\circ K \\ Pr &= 0.72 & \gamma &= 1.4 \end{aligned} \tag{6}$$

The cylinder had a diameter of 0.3048 m and a constant wall temperature of 556 $^\circ$K. The freestream Mach number and impinging shock angles were chosen to correspond with the three-dimensional tests of Edney (ref. 1) in which

planar shocks were allowed to impinge upon a hemisphere.

The undisturbed blunt body flow field was computed first and the resulting solution was used as the initial condition for the shock impingement computations. Wall pressure and heat transfer rates from this undisturbed case compared very well with independent results (ref. 3).

Two shock impingement cases are presented here with identical intersection positions, $\theta = 9^{\circ}$, but with different impinging shock strengths. In the first case the impinging shock made an angle of 16.1° with the freestream velocity vector. The pressure ratio across this impinging shock was 1.73 with a flow deflection angle of 5°. The results of this computation are shown in figure 2 as a set of Mach number contours which were drawn by a computer plotter in increments (ΔM) of 0.05. A strong shear layer emanates from the intersection point and makes a tangential approach to the body surface. This causes moderate increases in heat transfer and wall pressure in the vicinity of the attachment point. The lower sonic line position remains essentially unchanged from the no impingement case while the upper sonic line position is changed considerably. The new upper sonic line emanates from the intersection point and follows the shear layer to the body.

In the second two-dimensional case the impinging shock made an angle of 20.9° with the freestream velocity vector. The pressure ratio across this impinging shock was 2.98 with a flow deflection angle of 10°. The results of this computation are shown in figure 3 as a set of Mach number contours drawn in the same manner as figure 2. The bow shock distinctly shows a "double kink." A strong shear layer emanates from the intersection point (first kink) and strikes the body. An imbedded supersonic region exists between the shear layer and a shock emanating from the second kink

in the bow shock. The stagnation point has been shifted approximately 45^{o} around the cylinder by the impingement. It is at this new stagnation point where large increases in heat flux and wall pressure occur. The shock impingement also causes the bow shock standoff distance below the intersection point to increase dramatically.

Figure 4 shows a Schlieren photograph of the corresponding three-dimensional test of Edney. A qualitative comparison between the two-dimensional numerical and three-dimensional experimental results show the same general features, that is: 1) "double-kinked" bow shock, 2) shear layer emanating from the first kink and striking the body and 3) am imbedded shock emanating from the second kink in the bow shock. This good agreement gives credibility to the numerical computation.

Comparisons of the wall pressures and heat transfer rates before and after shock impingement are shown in figures 5 and 6 for the 20.9^{o} shock impingement case. Both curves represent numerical results as no experimental data was available for this set of conditions. The increases in wall pressure and heat transfer rate were both approximately 2.2 times greater than the no impingement stagnation point values.

Three-Dimensional

The preliminary three-dimensional solution presented in this paper was computed with the following freestream conditions:

$$\begin{aligned} M_{\infty} &= 5.94 & p_{\infty} &= 559.1\ N/m^2 \\ Re_{D\infty} &= 18{,}000 & T_{\infty} &= 59.6\ ^{o}K \\ Pr &= 0.72 & \gamma &= 1.4 \\ \lambda &= 25.0^{o} \end{aligned} \tag{7}$$

The cylinder was 0.025 m in diameter and had a constant wall temperature of 394 ^{o}K. The freestream conditions (except for $Re_{D\infty}$), impinging shock angle and sweep angle were all chosen to agree with the experiment of Keyes and Hains (ref. 2). The freestream viscosity was chosen to be an order of magnitude larger than in the experiment, thus making the Reynolds number ten times smaller. This was done to physically thicken the boundary layer and make its resolution possible with fewer grid points.

At the start of the shock impingement computation the flow variables in all z-planes were set equal to a previously computed swept infinite cylinder solution. Then, except for the flow variables at the inflow plane which were held fixed, the flow variables in all other planes were allowed to change during the computation under the influence of the impinging shock.

A comparison of the stagnation plane shock shapes is shown in figure 7. The results of Keyes and Hains were obtained by allowing a planar impinging shock to strike the shock layer on a finite swept cylinder. The intersection point along the stagnation plane was only three centimeters downstream from one end of the cylinder. The shock standoff distance for the initial numerical z-plane is therefore much different than the corresponding value of the experimental results. When these curves are examined in light of this difference the comparison seems quite good.

A comparison of the stagnation line wall pressures is shown in figure 8. The general trend of the comparison is reasonable. However, the peak value in the experimental curve, which is caused by a boundary layer interaction with a transmitted shock, is not reproduced in the numerical results. A small peak does occur in the numerical results but differs slightly in position with the experimental peak.

A comparison of the stagnation line heat transfer is presented in figure 9. A peak in the heating rate is measured for both the numerical and experimental results although the positions and heights of the peaks are not in good agreement. The coarse grid, numerical smoothing, and increased physical viscosity probably all contribute to the poor resolution of the transmitted shock and therefore, to the poor agreement. Future investigations will either remove or improve these limitations.

For this preliminary three-dimensional solution a coarse 21 x 21 x 41 grid was used requiring 90,405 words of array storage. The total program storage (program and array storage) was 120,000 words. The execution time on a CDC 7600 computer was 47 minutes.

CONCLUDING REMARKS

Both two- and three-dimensional shock impingement flow fields have been computed using a time-dependent finite-difference procedure to solve the complete set of Navier-Stokes equations. Good qualitative comparisons were obtained between two-dimensional numerical results and corresponding three-dimensional experiments. In addition, the ability to compute the preliminary three-dimensional solution demonstrated that the large computer demands associated with problems of this type can be overcome.

REFERENCES

1. Edney, B. E.: Anomalous Heat Transfer and Pressure Distributions on Blunt Bodies at Hypersonic Speeds in the Presence of an Impinging Shock. FFA Rept. 115, The Aeronautical Research Institute of Sweden, Stockholm, Sweden. February 1968.

2. Keyes, J. W.; and Hains, F. D.: Analytical and Experimental Studies of Shock Interference Heating in Hypersonic Flows. NASA TN D-7139, May 1973.

3. Tannehill, J. C.; Holst, T. L.; and Rakich, J. V.: Numerical Computation of Two-Dimensional Viscous Blunt Body Flows with an Impinging Shock. AIAA Paper No. 75-154, January 1975.

4. MacCormack, R. W.: The Effect of Viscosity in Hypervelocity Impact Cratering. AIAA Paper No. 69-354. April 1969.

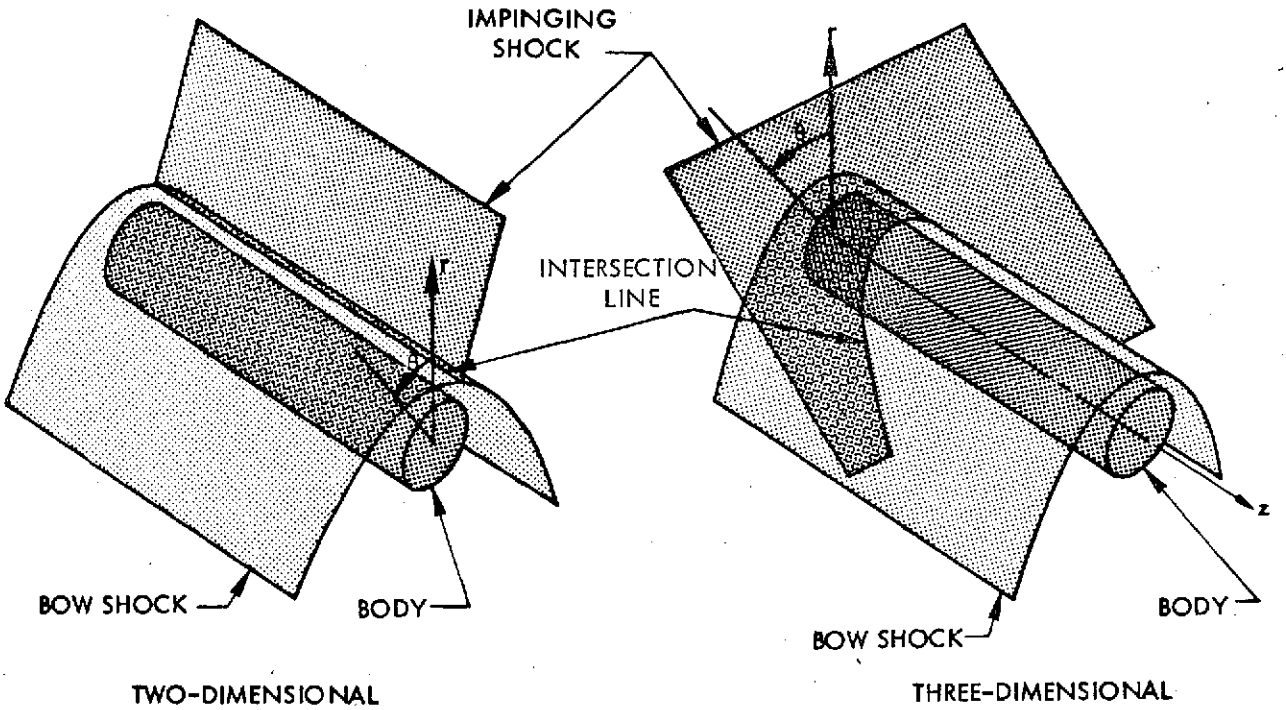

Figure 1.- Shock impingement geometries.

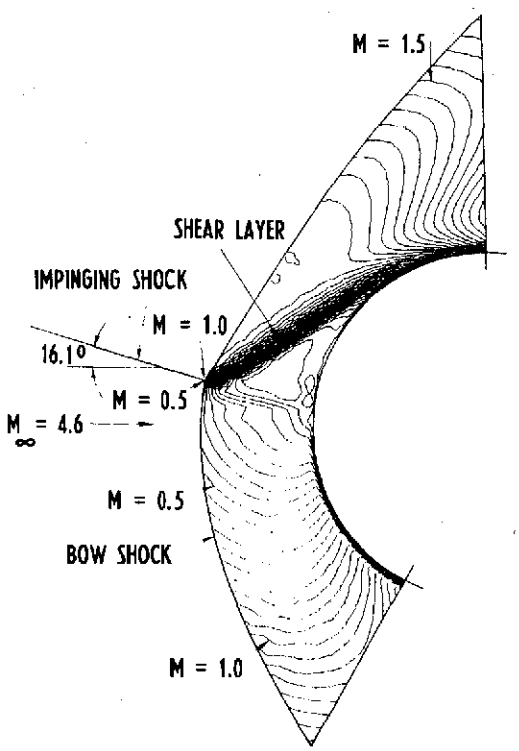

Figure 2.- Mach number contours for 16.1° shock impingement at $\theta = 9°$.

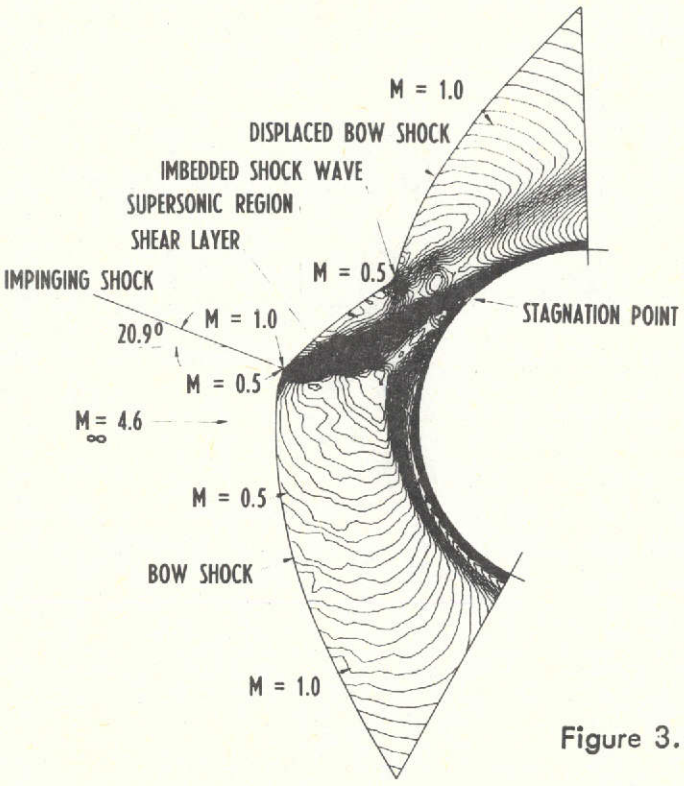

Figure 3. - Mach number contours for 20.9° shock impingement at $\theta = 9°$.

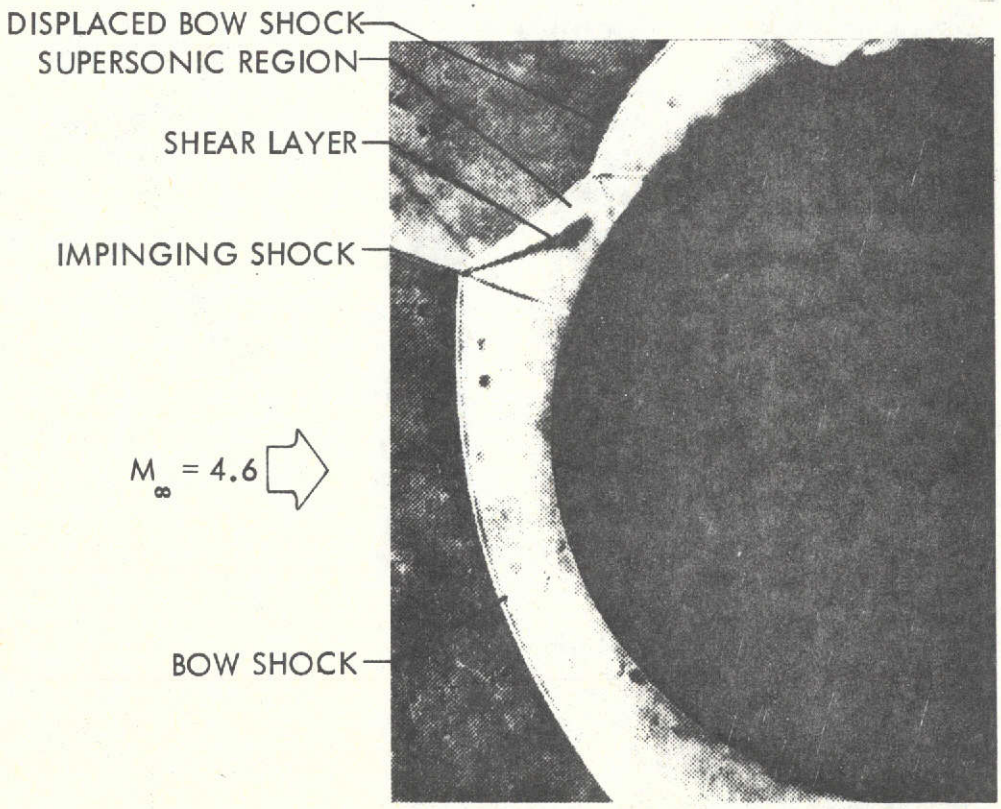

Figure 4. - Three-dimensional experimental result of Edney for 20.9° shock impingement.

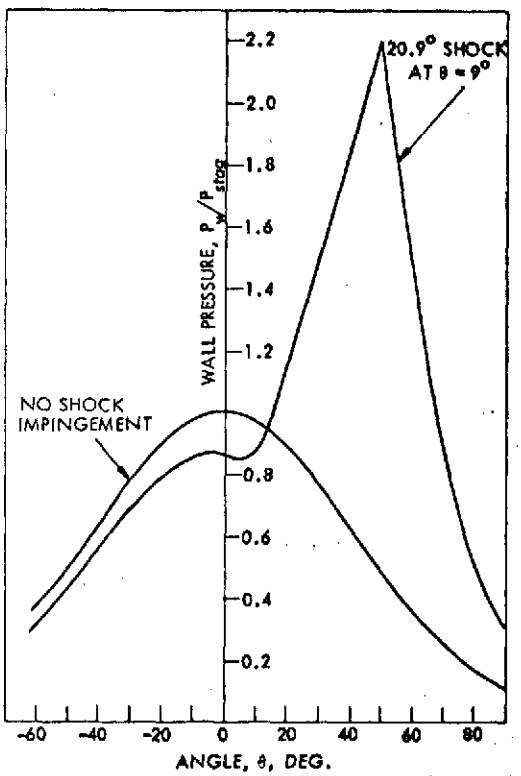

Figure 5.- Comparison of wall pressures.

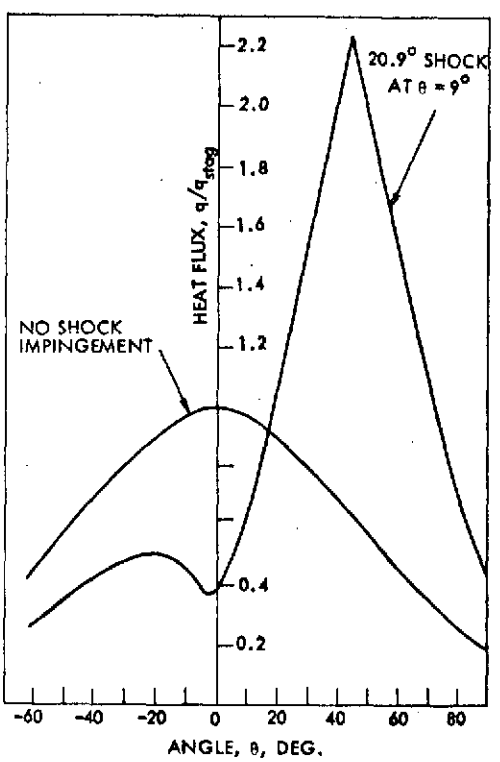

Figure 6.- Comparison of heat transfer rates.

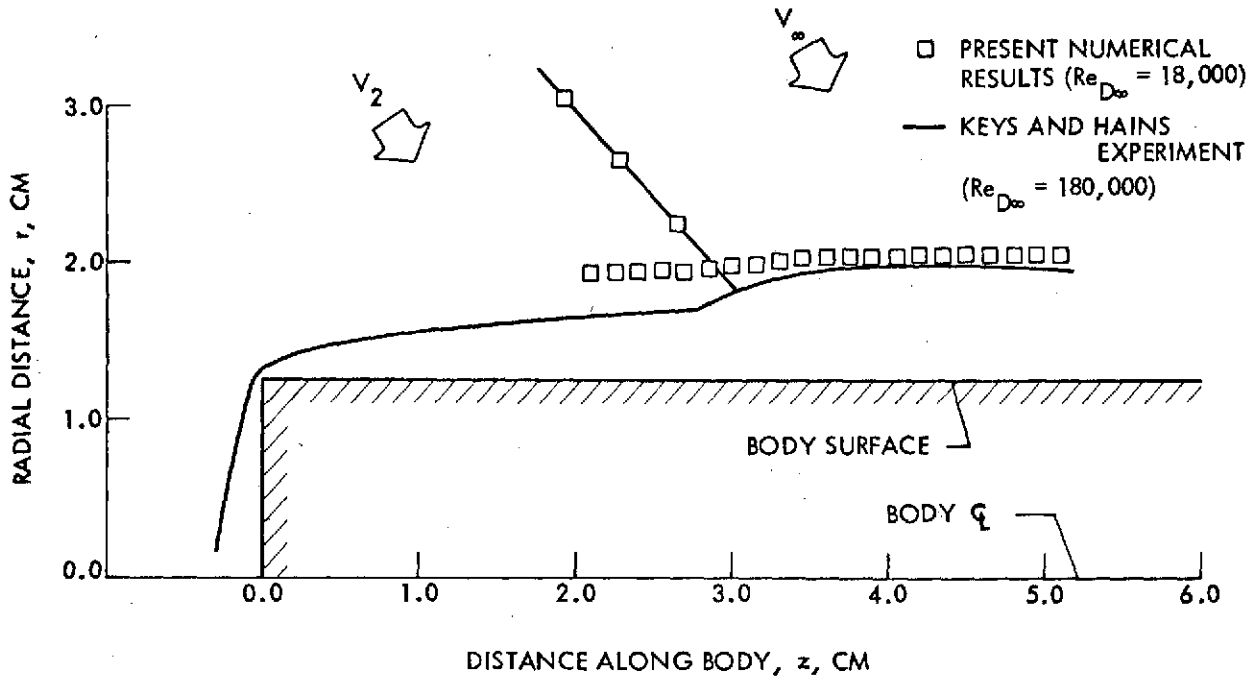

Figure 7. - Stagnation plane shock shape comparison.

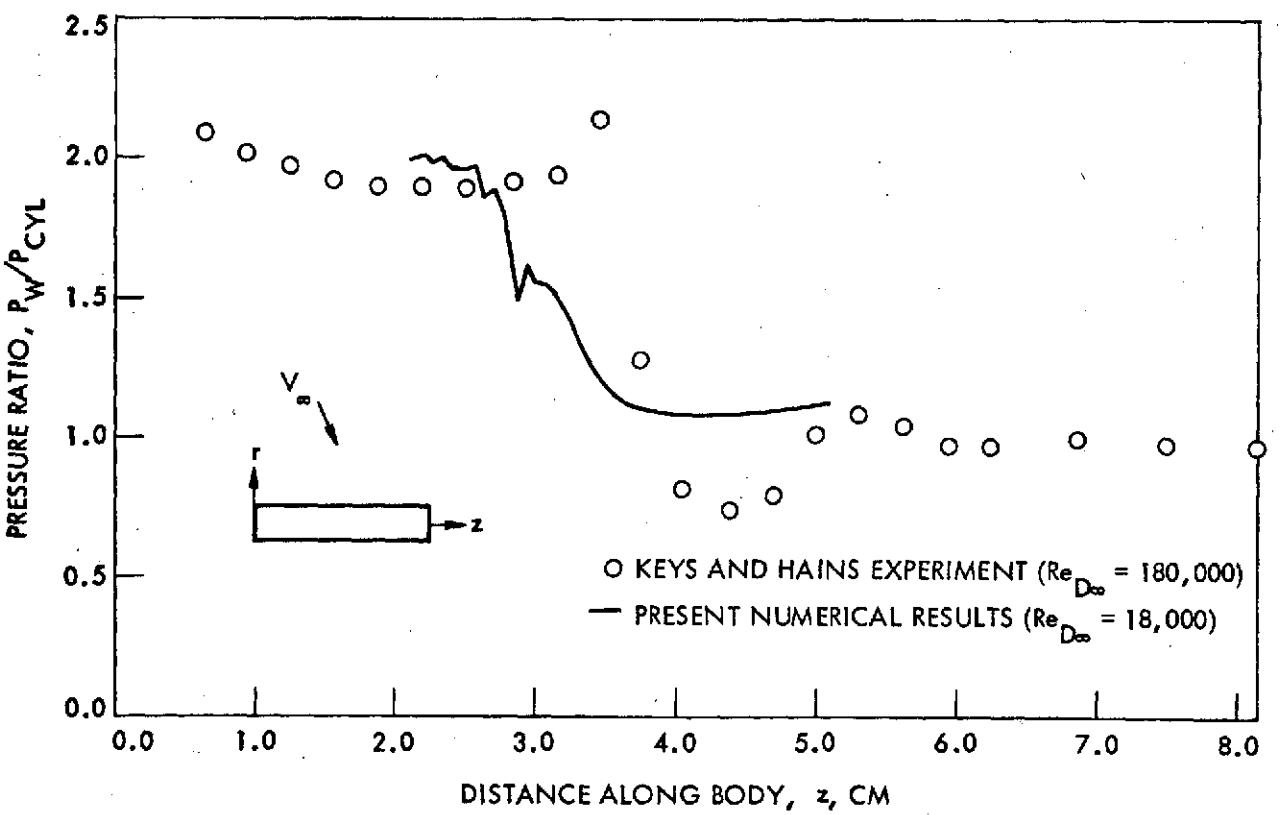

Figure 8. - Stagnation line wall pressure comparison.

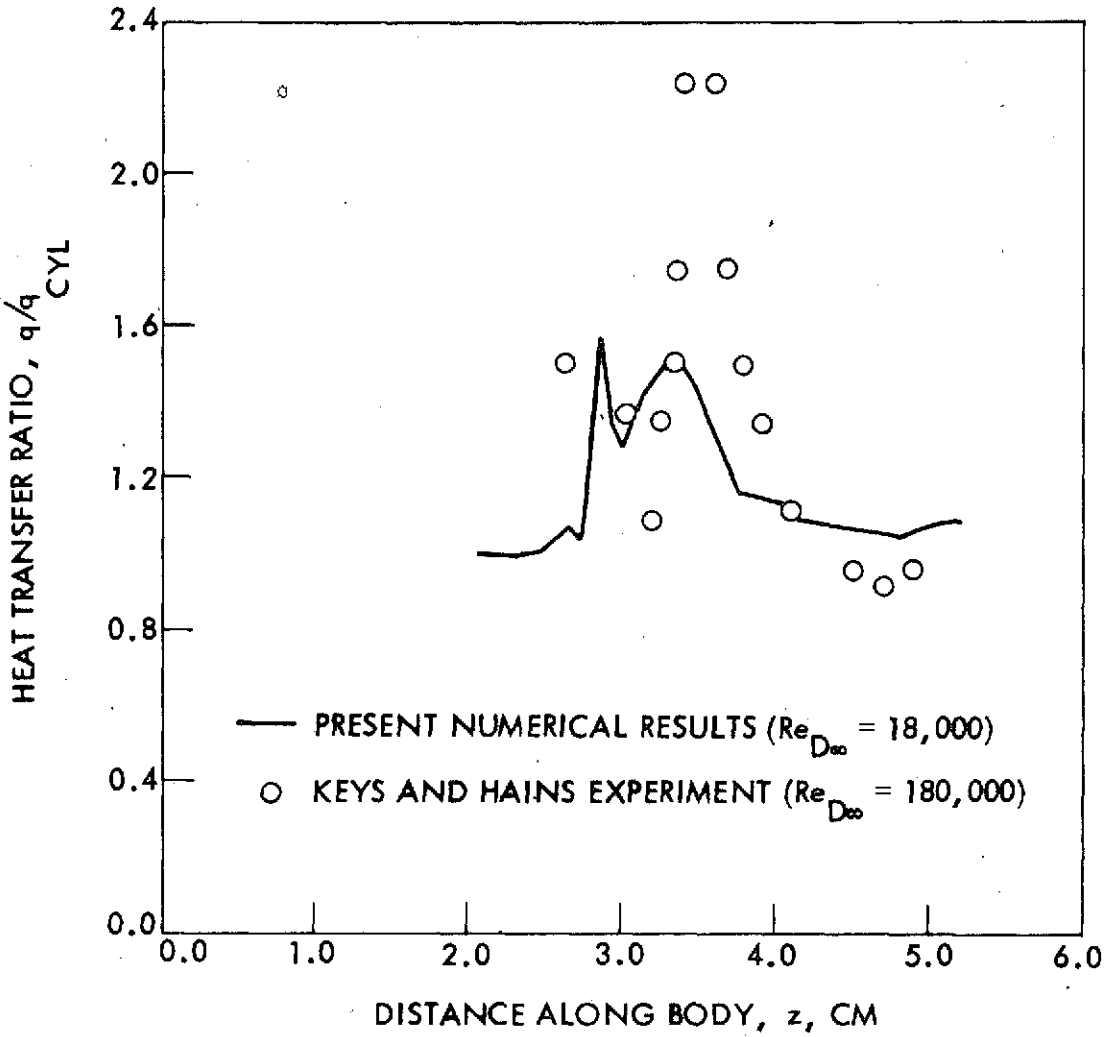

Figure 9.- Stagnation line heat transfer comparison.